AIROPA IV: Validating point spread function reconstruction on various science cases

Sean K. Terry ,[a,*] **Jessica R. Lu ,**[a] **Paolo Turri ,**[b] **Anna Ciurlo ,**[c]
Abhimat Gautam ,[c] **Tuan Do ,**[c] **Michael P. Fitzgerald ,**[c] **Andrea Ghez,**[c]
Matthew Hosek Jr.,[c] **and Gunther Witzel** [d]

[a]University of California, Berkeley, Department of Astronomy, Berkeley, California, United States
[b]University of British Columbia, Department of Physics and Astronomy, Vancouver, British Columbia, Canada
[c]University of California, Los Angeles, Division of Astronomy and Astrophysics, Los Angeles, California, United States
[d]Max-Planck-Institut für Radioastronomie, Bonn, Germany

Abstract. We present an analysis of six independent on-sky datasets taken with the Keck-II/ NIRC2 instrument. Using the off-axis point spread function (PSF) reconstruction software AIROPA, we extract stellar astrometry, photometry, and other fitting metrics to characterize the performance of this package. We test the effectiveness of AIROPA to reconstruct the PSF across the field of view in varying atmospheric conditions, number and location of PSF reference stars, stellar crowding, and telescope position angle (PA). We compare the astrometric precision and fitting residuals between a static PSF model and a spatially varying PSF model that incorporates instrumental aberrations and atmospheric turbulence during exposures. Most of the fitting residuals we measure show little to no improvement in the variable-PSF mode over the single-PSF mode. For one of the data sets, we find photometric performance is significantly improved (by ∼10×) by measuring the trend seen in photometry as a function of off-axis location. For nearly all other metrics we find comparable astrometric and photometric precision across both PSF modes, with a ∼13% smaller astrometric uncertainty in variable-PSF mode in the best case. We largely confirm that the spatially variable PSF does not significantly improve the astrometric and other PSF fitting residuals over the static PSF for on-sky observations. We attribute this to unaccounted instrumental aberrations that are not characterized through afternoon adaptive optics (AO) bench calibrations. © *The Authors. Published by SPIE under a Creative Commons Attribution 4.0 International License. Distribution or reproduction of this work in whole or in part requires full attribution of the original publication, including its DOI.* [DOI: 10.1117/1.JATIS.9.1.018003]

1 Introduction

With the next generation of adaptive optics (AO) instruments coming online soon, it is becoming increasingly important to properly characterize the spatial and temporal dependence of the point spread function (PSF) for data obtained with AO. The Keck-I and Keck-II AO systems have been used to deliver very-high-resolution imaging for well over two decades and have been continuously upgraded and fitted with newer-generation hardware. The future of both Keck telescopes is filled with several promising next-generation updates[1,2]

As a result of imperfect knowledge of the spatially varying (i.e., off-axis) PSF in these AO systems, very precise astrometry and photometry for a large majority of stellar sources in crowded fields (for example) has been limited. The Anisoplanatic and Instrumental Reconstruction of Off-axis PSFs for AO (AIROPA) is a suite of software packages that utilize phase-diversity measurements, atmospheric profile data, and wave propagation through both

*Address all correspondence to Sean K. Terry, sean.terry@berkeley.edu

turbulence and optical systems. With this knowledge, AIROPA generates a model of the field-dependent PSF for both natural guide star (NGS) and laser guide star (LGS) modes. The software functions under the assumption that every PSF that is extracted consists of a convolution of the on-axis PSF, the instrumental aberration, and the atmospheric anisoplanatism.[3] Further descriptions of AIROPA and the submodules that it is built upon are given in Ref. [4].

For context, we give a brief description of the input data needed for AIROPA. These data are used to generate the optical transfer function (OTF) grids (instrumental + atmospheric), on-axis and off-axis PSFs, and other files for the subsequent photometric and astrometric analyses. Instrumental aberration maps are generated by conducting fiber phase-diversity measurements at the detector plane for NIRC2 (see Secs. [2] and [3] of Ref. [5] for further details). A grid of phase maps is generated, where each map is the result of the difference between the measured on-axis wavefront and off-axis wavefront across the 1024×1024 pixel field. Since the instrumental phase maps are mostly static,[5] the instrumental OTF can be read from a predetermined library of OTFs at various rotator angles. This significantly increases efficiency and reduces computation time for a given AIROPA analysis. The multiaperture scintillation sensor (MASS) and differential image motion monitor (DIMM) are instruments on the summit of Mauna Kea that monitor the seeing and generate atmospheric profiles (C_n^2) at altitudes of 0.5, 1, 2, 4, 8, and 16 kilometers (km) above the summit. The algorithm that feeds this seeing information into AIROPA is called ARROYO,[6] and is built upon a set of C++ libraries. The AIROPA-generated OTF then represents the combination of the instrumental phase maps and atmospheric profile that are needed in order to construct the field-dependent PSF model. As outlined in Refs. [4] and [7], the AIROPA PSF model can be described as the convolution of the on-axis PSF with an instrumental and atmospheric component to characterize its spatial variability

$$\mathrm{PSF}(r,t) = \mathrm{PSF}_0(t) \otimes \mathrm{PSF}_{\mathrm{inst}}(r,t) \otimes \mathrm{PSF}_{\mathrm{atm}}(r,t). \tag{1}$$

For convenience, a Fourier transform of the PSF is performed to obtain the OTF via the convolution theorem

$$\mathrm{OTF}(r,t) = \mathrm{OTF}_0(t) \times \mathrm{OTF}_{\mathrm{inst}}(r,t) \times \mathrm{OTF}_{\mathrm{atm}}(r,t), \tag{2}$$

where $\mathrm{OTF}_{\mathrm{inst}}$ and $\mathrm{OTF}_{\mathrm{atm}}$ are the ratios of the OTF at the position r with respect to the on-axis OTF_0, which is caused by instrumental aberrations and atmospheric anisoplanatism.

The PSF extraction and fitting is performed on each science image and final star lists are generated with photometry and astrometry for each detected source. Additionally, we rely on a fitting metric deemed the fraction of variance unexplained (FVU), for determining how well the PSF model has fit the data in each image. A simplified form is given as

$$\mathrm{FVU} = \frac{\sigma_{\mathrm{res}}^2}{\sigma_{\mathrm{img}}^2}, \tag{3}$$

where σ_{res}^2 is the variance of the residual and σ_{img}^2 is the variance of the image for a particular source (star). A detailed description of the calculation and full-form equation are given in Sec. [3.2] of Ref. [5]. For a schematic of the variable-PSF algorithm in AIROPA, we refer to Fig. 1 in Ref. [7]. The first iteration in the pipeline determines the initial catalog of sources. Further, the reconstructed PSFs are cross-correlated with the image to find all suitable stars and to reject poorly fit sources such as speckles, galaxies, or cosmic rays. The source catalog is then refined by iterating over the grid of reconstructed PSFs and minimizing the least squares error between the data and the model.

This study is the fourth in a series of papers detailing the AIROPA package;[4] introduces AIROPA and gives an overview of the software structure. Characterization of the Keck-II/NIRC2 instrumental aberrations and AIROPA's usage of this aberration data is given in Refs. [5] and [7] to perform tests of AIROPA on simulated and on-sky Galactic Center (GC) images. In this paper, we focus on expanding the on-sky tests of AIROPA. The paper is organized as follows: Sec. [2.1] describes the analysis of a very crowded field through three independent GC datasets. In Sec. [2.2], we describe a less-crowded field for a typical high-resolution gravitational

microlensing science case. In Sec. 2.3, we detail the observations of globular cluster Messier 53 (M 53) taken at various position angles (PA). In Sec. 3, we compare the photometric, astrometric, and FVU results for each science case. Finally, we give a discussion and conclude the paper in Sec. 4.

2 Observations

All datasets presented in this work were acquired on Keck-II with the near-infrared camera 2 (NIRC2) narrow camera instrument in LGS adaptive optics (LGSAO) mode and with the Kp filter ($\lambda_c = 2.12$ μm). The plate scale for the NIRC2 narrow camera is 9.952 mas/pix,[8] and all the data were taken between May 2015 and August 2017.

A total of six cleaned frames from each dataset were reduced identically with a NIRC2 pipeline that corrects for differential atmospheric refraction (DAR), bad pixels, cosmic rays, and other undesirable effects[9,10] and applies geometric distortion corrections.[8,10] North is up and east is left in all observations, with one exception for the PA = 90 deg observations where east is up and south is left [Fig. 1(a)]. Figure 1 shows the median Strehl ratio (SR) and full-width half maximum (FWHM) values and standard deviations for all datasets analyzed in this work. Figure 1(b) shows the atmosphere profile information from the DIMM/MASS instruments for each dataset, with gray-shaded regions representing the time of observation considered in this analysis. The observation timestamps span 8:30 pm to 4:30 am local Hawaiian Standard Time (HST). Table 1 shows the quality metrics: median SR, FWHM, and root-mean-square deviation of the wavefront error (RMS WFE). The table also gives observation dates and total exposure times for all datasets.

There are many reasons to include a wide range of variable condition data across different stellar fields on-sky, which include testing the effects of varying DIMM/MASS profiles on PSF extraction (Sec. 2.1), testing the fitting precision on datasets with more (or less) PSF reference stars in the field (i.e., crowded or sparse fields, Secs. 2.2 and 2.3), and determining the reliability of goodness-of-fit and other PSF fitting residuals for extracted sources (Secs. 3.1 and 3.2).
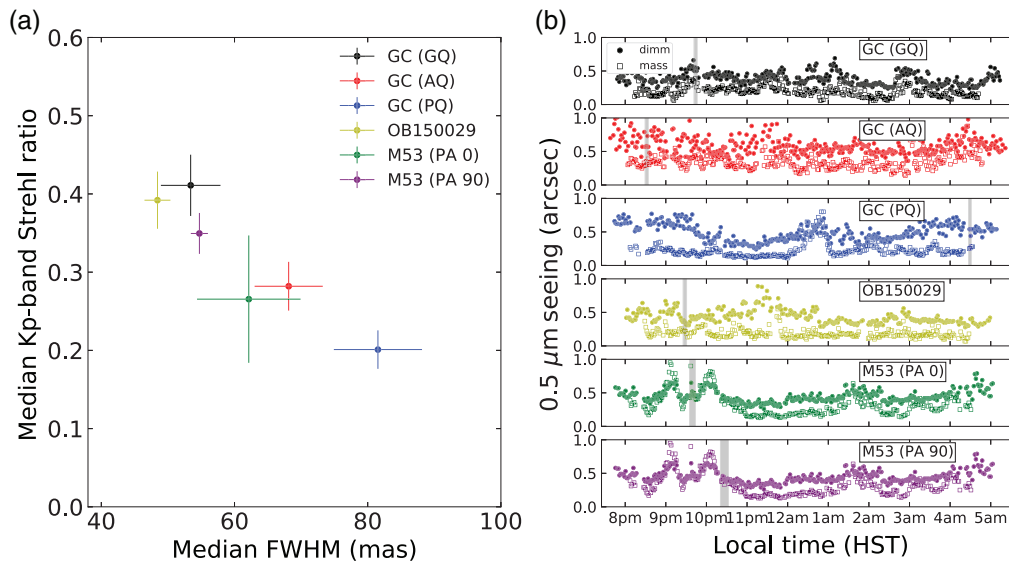
Fig. 1 (a) Median SR and FWHM values for all datasets analyzed in this work. Error bars represent the standard deviation across the temporal data set (e.g., six frames). Single-valued SR and FWHM are estimated for each image by our reduction pipeline. (b) 0.5 μm DIMM/MASS seeing profiles for each dataset, respectively. Gray shaded region represents the time of observation for each set.

**Table 1** Observational data presented in Secs. 2.1, 2.2, and 2.3.

Field	Date (UT)	Strehl ratio (**K**p-band)	FWHM (mas)	RMS WFE (nm)	Exp. time (s)
GC (GQ)	August 11, 2017	0.41 ± 0.039	53 ± 4.5	320 ± 18	168
GC (AQ)	August 23, 2017	0.29 ± 0.024	66 ± 3.5	380 ± 13	168
GC (PQ)	May 03, 2016	0.21 ± 0.025	82 ± 6.6	430 ± 18	168
OB150029	July 14, 2016	0.39 ± 0.037	48 ± 1.9	330 ± 17	180
M53 (PA 0)	May 05, 2015	0.27 ± 0.081	62 ± 7.8	390 ± 44	300
M53 (PA 90)	May 05, 2015	0.35 ± 0.026	55 ± 1.3	350 ± 12	300

2.1 Comparing Atmospheric Conditions in a Very Crowded Field: The Galactic Center

We expand upon the initial on-sky GC testing of Ref. 7 by including "good quality," "average quality," and "poor quality" datasets (hereafter GQ, AQ, and PQ, respectively) for further AIROPA validations on the GC. The GC case was used as the main science driver for the original development of AIROPA. This case is ideal since there already exists a rich high-resolution dataset spanning several decades, dozens of reference stars for PSF modeling, and a very bright, uniform tip/tilt (TT) star that is ~13 arcsec arcsec off-axis. The longest-running high-resolution study of the stellar population immediately surrounding SgrA* is being conducted by the Galactic Center Orbit Initiative.[11] This work has led to a deep and well-understood knowledge[9,10,12–14] of the environment immediately surrounding the central supermassive black hole.

We rank the three GC datasets, GQ, AQ, and PQ based on the historical quality of all GC epochs taken with NIRC2 since 2004.[15] Note that our definition of "good," "average," and "poor" involves more than just the atmospheric conditions during those datasets. The overall image quality can be affected by multiple contributing factors related to atmospheric conditions, stability and performance of the AO system on a given night, brightness and variation of TT/guide stars, or the Strehl/FWHM reference star selection.

The GQ data were taken on August 11, 2017, the AQ data were taken ~2 weeks after the GQ data, on August 23, 2017, and the PQ data were taken on March 05, 2016. For all GC datasets, each frame was composed of 10 coadded exposures at 2.8 s per coadd for a total exposure time of 28 s per frame. One note about the PQ dataset – there does not exist phase-diversity calibration data from 2016, therefore the 2017 instrumental phase maps were used to substitute for the 2016 phase maps. This is not an issue, as Ref. 5 shows that the phase maps can remain stable across multiple years, and any potential difference between 2016 and 2017 phase-diversity is likely small enough for an analysis of the kind presented in this work. Figure 2 shows one frame from
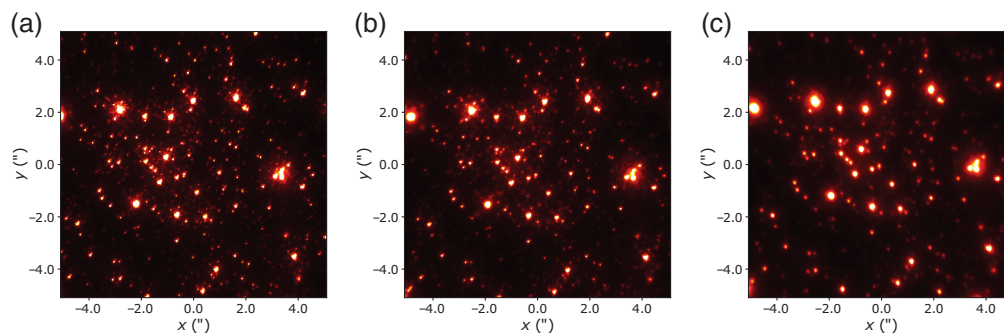

Fig. 2 (a) Good-quality Galactic Center frame. (b) Average-quality Galactic Center frame. (c) Poor-quality Galactic Center frame. All images have the same color scale, the axes represent on-sky separation (in arcsecond) from the LGS position. North is up and East is left in all frames.
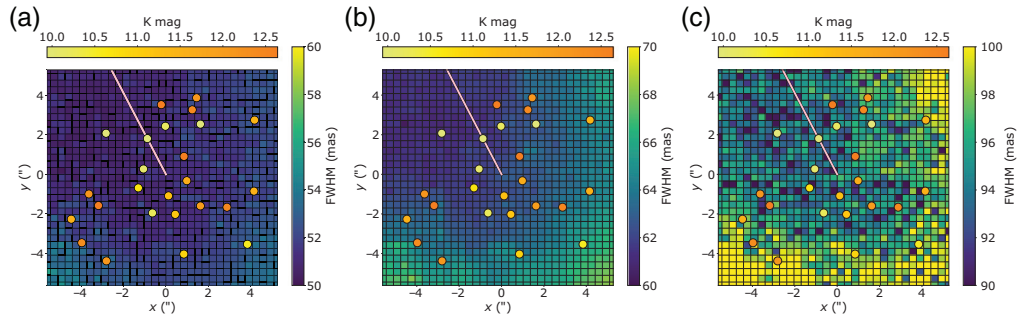
Fig. 3 Grid of FWHM values from AIROPA variable-PSF mode on (a) the GQ, (b) AQ, and (c) PQ datasets. Colored circle data points correspond to locations and K-band magnitudes of primary PSF reference stars. A solid line connects the on-axis LGS position to the off-axis TT guide star position.
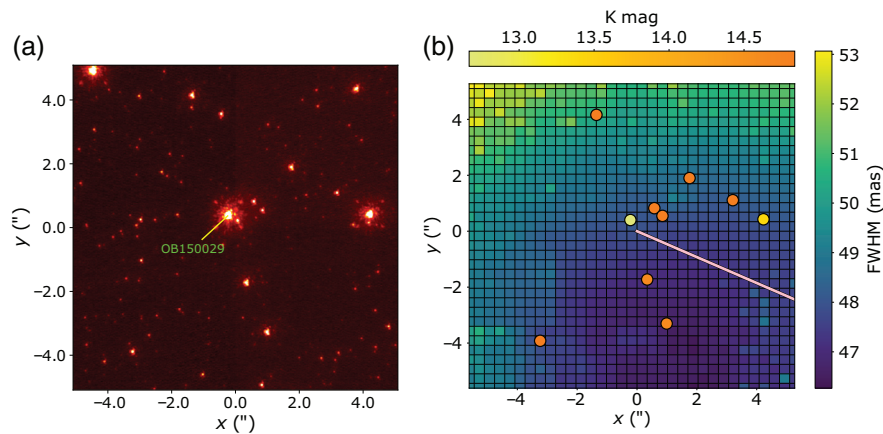

Fig. 4 (a) NIRC2 frame of the OB150029 field taken on July 14, 2016, with the Kp filter. (b) FWHM grid from AIROPA variable-PSF mode with selected PSF reference stars colored by magnitude and solid line connecting the on-axis position to the TT guide star.

each of the three epochs, with the spatial scale given as the separation (in arcseconds) from the on-axis position (i.e., location of the LGS). We note that there are two other axes of importance; the direction of the TT star (given by the solid line in Figs. 3–5), and the position of the image sharpening (typically offset from the center of the image). Figure 3 shows the grid of FWHM values measured by AIROPA variable-PSF mode for each frame, plotted over the field of view to give a visualization of the field-dependent PSF. The FWHM grid values are calculated for every PSF generated by AIROPA in a PSF grid file. The AIROPA grid files for the fields analyzed in this work use a partition size (i.e., step width of the PSF grid) of 102.

2.2 Less Crowded Field: OGLE-2015-BLG-0029

The optical gravitational lensing experiment (OGLE) survey[16] conducts wide-field visible and near-IR imaging of nearly the entire Galactic Bulge region at high cadence and detects over 1000 microlensing events every season. Most ground-based imaging data from current microlensing surveys are focused on the regions $3\ \mathrm{deg} > l > 357\ \mathrm{deg}$ and $-2.5\ \mathrm{deg} < b < 2.5\ \mathrm{deg}$. The first non-GC data analyzed in this work is OGLE-2015-BLG-0029 (hereafter OB150029), located at RA = 17:59:46.60, dec = –28:38:41.80 and Galactic coordinates $(l, b = (1.828\ \mathrm{deg},\ -2.523\ \mathrm{deg}))$ in J2000 epoch. This target has been regularly monitored with NIRC2 since 2015 as part of a project to study isolated stellar-mass black hole candidates.[17]

The OB150029 observations were taken on July 14, 2016 in LGSAO mode with the Kp filter. Each of the frames consist of six coadded images, each with five second integration time, for a total integration time of 30 s per frame. The airmass during the six-frame observing window was
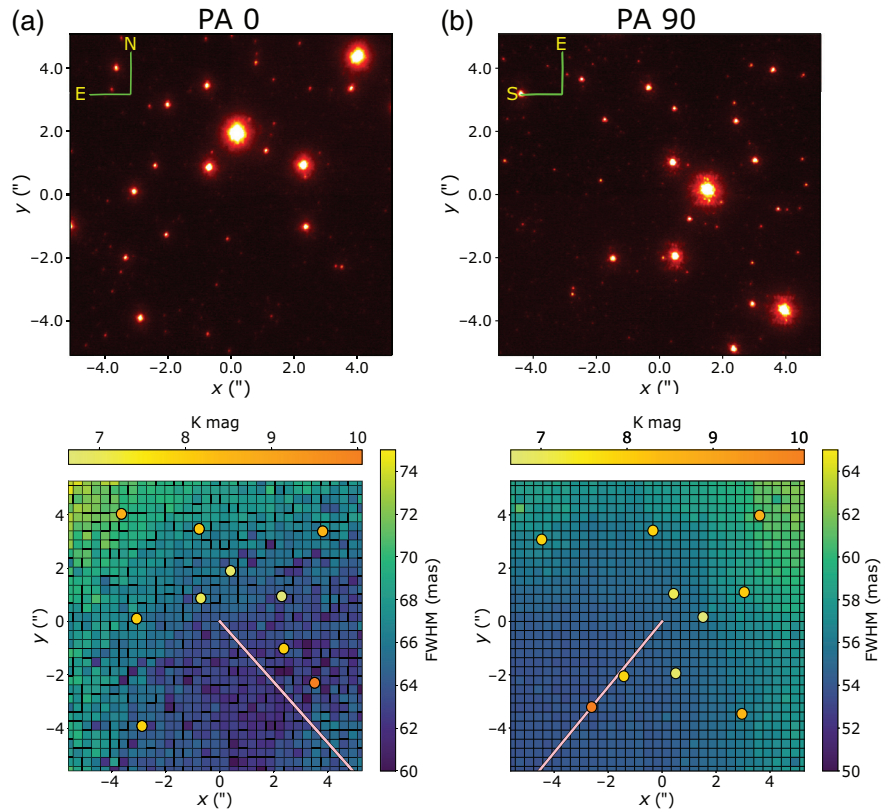
Fig. 5 (a) M53 NIRC2 frame taken at PA = 0 deg, with accompanying FWHM grid generated by AIROPA. (b) Same as left, but for PA = 90 deg. The solid line connects the on-axis LGS position to the TT guide star. The color scale is identical for both images in the top row.

~1.65, and the median SR, FWHM, and RMS WFE values for the six frames are given in Table 1, as well as the DIMM/MASS data given in Fig. 1(b). This is the second-best dataset (behind GQ) in terms of quality metrics like the median SR and FWHM and their variances across all six frames. Similar to the PQ dataset, there are no 2016 phase maps available for NIRC2, therefore, the 2017 maps were substituted. Again, phase-diversity measurements have shown these maps to be stable within ~59 nm RMS across several years.[5] Figure 4 shows a NIRC2 image of the field, which is clearly less crowded than the GC, particularly in the bright star regime.

There are a total of 10 PSF reference stars in this field that were used for AIROPA, compared to a total of 25 PSF reference stars used for the GC analysis described in Sec. 2.1. The total number and spatial location of selected PSF reference stars is important for constructing accurate PSF models, and the 10 stars chosen for the OB150029 field include the microlensing target itself (i.e., brightest star in the field), as well as stars within 1.5 mag of the target, and separations of ±4 arcsec from the target. The TT guide star used for the observations has an R mag ~15.1 and separation of ~13.8 arcsec to the south-west of the target, as indicated by the solid line in Fig. 4(b).

2.3 Comparing Different Position Angles: Globular Cluster M53

The globular cluster M53 (NGC 5024) located at RA = 13:12:54.51, dec = 18:10:13.95 (J2000) was observed with the NIRC2 narrow camera Kp filter on May 04, 2015, as part of a project to characterize the NIRC2 geometric distortion.[8] This was accomplished by comparing the NIRC2 stellar positions to precise astrometry from Hubble Space Telescope (HST) Advanced Camera for Surveys (ACS) observations.[18] The NIRC2 camera and AO system were realigned in April 2015, and observations of M53 before and after this realignment show an increase in the average geometric distortion from ~0.5 mas prerealignment to ~1.1 mas postrealignment.

Importantly for the current study, the M53 NIRC2 observations were taken at two different PAs; 0 deg and 90 deg. These observations present a unique dataset for us to compare the astrometric accuracy between single-PSF and variable-PSF modes in AIROPA as a function of PA. The previous study of Ref. 8 assumed a static PSF to derive the geometric distortion solution, which implies that using a variable-PSF on NIRC2 datasets will likely show residual distortion that was not modeled out by the static PSF used to derive the solution. Depending on the significance of this effect, some fraction of the difference in astrometric, photometric, or FVU results between the PSF modes may be attributed to this (Figs. 6, 10, 11, and 14). Due to the gradient in the NIRC2 distortion solution, the local pixel scale changes across the detector. This change, however small, is not detected in any PSF modeling because the aberration maps that are used are tip-tilt removed. This is very likely only a minor effect. As our intention in this paper is not to fully derive a new geometric distortion solution (with single and/or variable-PSF), we select only a subset of M53 NIRC2 images to remain consistent with the number of GC and microlensing frames used in previous sections. While it may prove beneficial to fully derive a new independent variable-PSF distortion solution for NIRC2, this is beyond the scope of the current paper. As shown in Ref. 7 and Fig. 6, the astrometric differences between single-PSF mode and variable-PSF mode become more severe at larger radii from the central on-axis position. This is predominantly caused by the difference in PSF shape between the spatially varying model and the static model, particularly closer to the sides and edges of the NIRC2 frame.

The M53 dataset includes six frames taken at a PA of 0 deg (north up, east left), and six frames taken at a PA of 90 deg (east up, south left). The PA = 0 deg dataset consists of four frames taken at the central pointing, and two frames were taken after a dither of
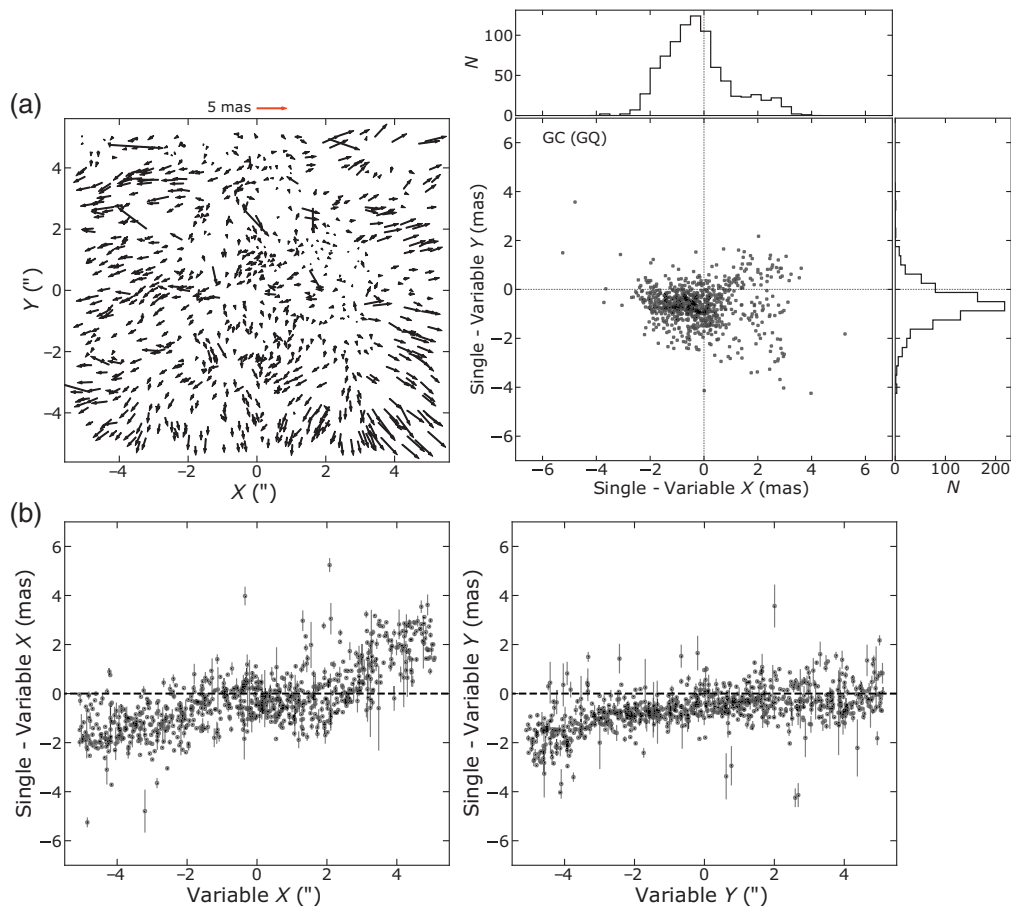
Fig. 6 (a) 2D positional difference in single versus variable PSF modes. Quiver plot shows positional differences as a function of field location. (b) 1D positional differences with errors derived from the RMS deviation of six positional measurements.

$\Delta_x = -0.14''$, $\Delta_y = 0.16''$. The PA $= 90$ deg dataset consists of four frames taken at the central pointing, and two frames were taken after a dither of $\Delta_x = +0.14''$, $\Delta_y = -0.19''$. The total exposure time is 50 s per frame for both PAs. Figure 5 shows one frame taken at PA 0 deg and the accompanying grid of FWHM values from AIROPA variable-PSF mode, as well as a PA 90 deg frame and FWHM grid. The same 10 PSF reference stars were used for each PA, as well as the same TT guide star, which has magnitude $R \sim 13.5$ located 24 arcsec to the south-west (solid line in the lower panels of Fig. 5).

3 Results

We present the AIROPA single-PSF and variable-PSF results for each field analyzed. As mentioned earlier, to maintain consistency we selected a subset of six consecutive frames from each dataset and used the averaged astrometry, photometry, and FVU in our final analysis and comparisons. All of the selected GC data (as well as the microlensing data) have exactly one dither between the first three frames and last three frames, while the M53 data have exactly one dither between the second and third frames (i.e., first two frames at one dither position, last four frames at a subsequent dither position).

There are three primary metrics that we used to assess the performance of each PSF mode in AIROPA, these are the photometric uncertainty, astrometric uncertainty, and FVU of the residual image at the given position. We do expect the varying conditions, data quality, PSF reference stars, and stellar crowding to impact AIROPA's effectiveness to reconstruct the PSF. Along with instrumental aberrations and atmospheric anisoplanatism, the combination of these factors (on the instrument and on-sky) work to effectively increase the overall noise present in the reconstructed PSFs, stellar profiles, and extracted photometry, astrometry, and FVU. For each dataset, a relative comparison of these metrics between the PSF modes will reveal any differences in the overall PSF-R performance or results for each mode.

In addition to the three primary metrics mentioned above, we also compare the M53 astrometry and photometry from each PSF mode to several external catalogs. We make these comparisons in an attempt to determine which PSF mode gives results that are more consistent with an external reference. As shown in Figs. 6 and 7, and in Ref. 7, there is a clear relative difference in astrometry and photometry between the two PSF modes in AIROPA. However, information on
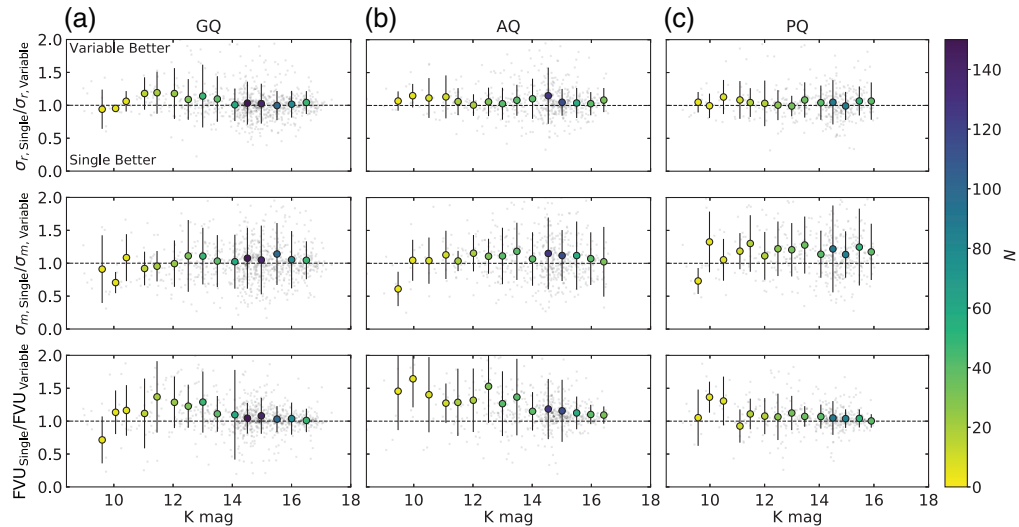
Fig. 7 Ratio of astrometric errors, photometric errors, and FVU values for the GC datasets; (a) GQ, (b) AQ, and (c) PQ. Values larger than one indicate the variable-PSF mode resulted in smaller astrometric/photometric residuals and smaller FVU, respectively. All stars are plotted in faint gray. Filled data points are colored by the number of stars in each 0.5 mag bin. Error bars give the 1σ standard deviation of the respective ratios in each bin.

Table 2 Photometric, astrometric differences in single, and variable PSF modes for bright sources $m \leq 13$.

Field	N_{bright}	$\Delta m_{(S-V)}$ [mag]		$\Delta r_{(S-V)}$ [mas]	
		$r \leq 3''$	$r > 3''$	$r \leq 3''$	$r > 3''$
GC (GQ)	140	-0.05 ± 0.02	0.01 ± 0.03	0.08 ± 0.52	1.01 ± 0.75
GC (AQ)	127	-0.03 ± 0.03	0.02 ± 0.05	0.08 ± 0.74	1.01 ± 0.98
GC (PQ)	112	-0.02 ± 0.02	0.03 ± 0.04	0.07 ± 0.84	0.76 ± 1.25
OB150029	19	0.03 ± 0.02	0.09 ± 0.04	0.12 ± 0.39	1.02 ± 0.56
M53 (PA 0)	32	-0.01 ± 0.04	0.04 ± 0.05	0.15 ± 0.68	0.95 ± 0.96
M53 (PA 90)	28	0.02 ± 0.03	0.10 ± 0.05	0.12 ± 0.68	0.55 ± 1.40

relative differences alone does not tell us which PSF mode produces results that are closest to truth. This requires comparisons like those described in the subsequent M53 results sections.

The various astrometry, photometry, FVU, and source color results are presented in several tables throughout the results section. Table 2 reports the difference in measured magnitudes and source positions in the two PSF modes. The stars and subsequent measurements are grouped into two radii; $r \leq 3''$, where the anisoplanatic effect on the PSFs should have a smaller impact, and $r > 3''$, where anisoplanatism significantly affects the shape of PSFs. Ideally, a spatially varying reconstructed PSF (i.e., AIROPA variable-PSF mode) properly accounts for the anisoplanatic effect by shaping the modeled PSF according to the instrumental and atmospheric components of the OTF at the larger off-axis locations. Table 3 gives the average photometric and astrometric errors, and average FVU results for all datasets analyzed in this work. The table includes results for all detected stars in each set, as well as results for the brightest stars ($m_K < 13$), as the PSF

**Table 3** Average photometric, astrometric uncertainties, and FVU results for each dataset.

Field	PSF Mode	$\bar{\sigma}_m$ [mag]		$\bar{\sigma}_r$ [mas]		$\langle \text{FVU} \rangle$	
		All	$m_K < 13$	All	$m_K < 13$	All	$m_K < 13$
GC (GQ)	Single	0.036	0.018	0.815	0.472	0.047 ± 0.070	0.005 ± 0.017
	Variable	0.036	0.019	0.806	0.427	0.047 ± 0.070	0.005 ± 0.017
GC (AQ)	Single	0.040	0.021	1.111	0.732	0.050 ± 0.062	0.011 ± 0.030
	Variable	0.039	0.021	1.069	0.711	0.045 ± 0.057	0.008 ± 0.022
GC (PQ)	Single	0.047	0.033	1.350	1.012	0.046 ± 0.052	0.012 ± 0.018
	Variable	0.042	0.028	1.327	0.962	0.045 ± 0.051	0.011 ± 0.018
OB150029	Single	0.037	0.032	0.613	0.454	0.105 ± 0.079	0.021 ± 0.021
	Variable	0.035	0.031	0.622	0.424	0.101 ± 0.078	0.019 ± 0.019
M53 (PA 0)	Single	0.068	0.063	1.071	0.670	0.162 ± 0.147	0.037 ± 0.059
	Variable	0.049	0.045	1.040	0.626	0.167 ± 0.156	0.036 ± 0.057
M53 (PA 90)	Single	0.051	0.036	0.962	0.306	0.202 ± 0.162	0.002 ± 0.001
	Variable	0.059	0.039	0.972	0.307	0.215 ± 0.176	0.002 ± 0.001

Note. Average photometric uncertainty in magnitudes is given by $\bar{\sigma}_m$ (columns 3-4), average astrometric uncertainty in milliarcseconds is given by $\bar{\sigma}_r$ (columns 5-6). The mean FVU and 1σ error is given in columns 7-8.
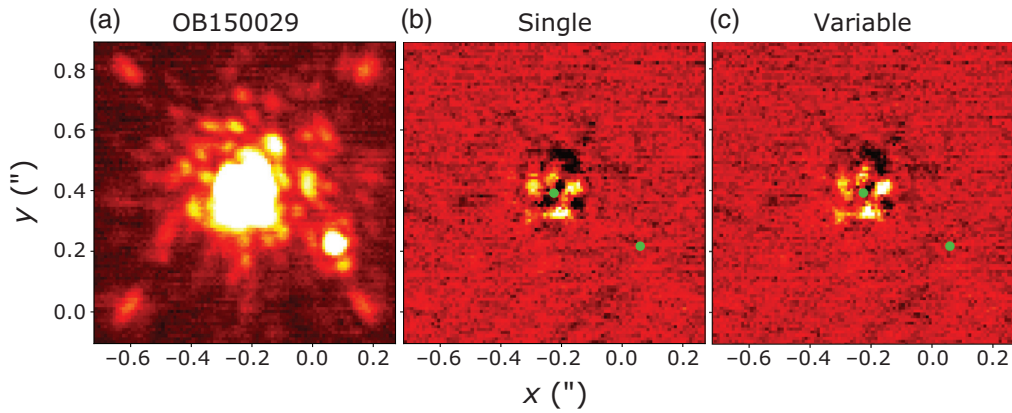
Fig. 8 (a) Zoomed image of the target OB150029, (b) residual images from the single-PSF, and (c) variable-PSF modes. Residual images have identical color scales, and green points show the location of star detections.
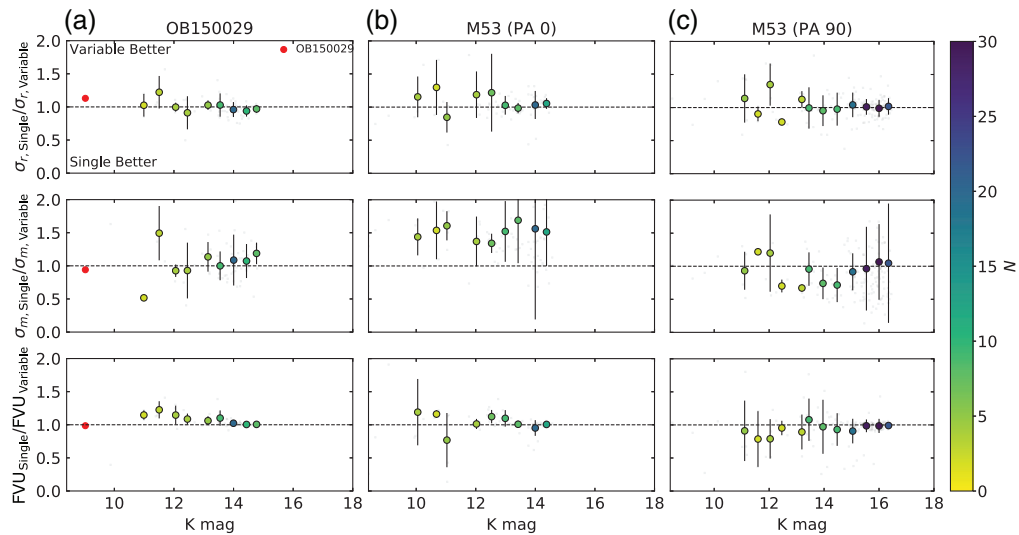
Fig. 9 Same as Fig. 7, but for (a) OB150029, (b) M53 PA 0, and (c) M53 PA 90.

residuals at the brightest magnitudes are affected primarily by PSF systematic errors rather than noise.[7] This effect can be seen in the FVU comparisons for bright stars in each field (Figs. 7–9 and the right columns in Table 3).

3.1 Galactic Center

For the very crowded GC datasets, identical reductions and analyses were performed across each of the six-frame sets. The same 25 PSF reference stars were used in each analysis and the astrometric, photometric, and FVU results are given in the following three subsections. Note that for each of the three datasets, we impose a requirement that in order for a star to be included in the analysis, it must be detected in at least five of the six cleaned frames.

3.1.1 GC: Good quality (GQ)

The GQ dataset contains the largest number of stars detected of all data analyzed in this paper. A total of 840 stars were detected in at least five of the six GQ frames. Figure 6 shows the averaged difference (from the six frames) between the measured star positions in single-PSF

and variable-PSF modes. The astrometric differences are largest at off-axis locations farthest from the frame center, in part due to the difference in PSF shape between the static and the spatially variable PSF models. Figure 6(a) shows the field position for each detected star and the corresponding 2D position difference on the detector plane. The 1D differences are shown in Fig. 6(b). The mean astrometric difference in each direction across the detector for bright stars inside and outside of a 3″ off-axis radius is given in Table 2, along with the mean magnitude differences.

The average photometric and astrometric precision for all GQ stars in both PSF modes is $\sigma_m \sim 0.04$ mag and $\sigma_r \sim 0.81$ mas, respectively. Further, the average FVU metric is very similar for the variable-PSF mode (4.67×10^{-2}) and single-PSF mode (4.70×10^{-2}). There may be evidence of some improvement in the astrometric errors and FVUs for only the brightest stars in the field [i.e., Fig. 7(a)], but any possible improvement here is significantly less than what has been measured on simulation tests.[7]

3.1.2 *GC: Average quality (AQ)*

The total number of stars detected across the AQ frames is 576, ∼30% less than the GQ dataset. As expected, the average uncertainties are marginally larger than those from the GQ dataset. When comparing the results from both PSF modes, we measure marginally smaller uncertainties for the variable-PSF mode over the single-PFS mode. While these results imply that variable-PSF is performing better than single-PSF mode, we note again that these improvements are still well below what has been shown through simulated data tests.

The average photometric precision for the AQ stars is $\sigma_m \sim 0.038$ mag for variable-PSF mode and $\sigma_m \sim 0.040$ mag for single-PSF mode. Further, the measured astrometric precision is $\sigma_r \sim 1.07$ mas for variable-PSF mode and $\sigma_r \sim 1.11$ mas for single-PSF mode. Finally, the average FVU metric is smaller (∼10%) for the variable-PSF mode (4.52×10^{-2}) compared to single-PSF mode (5.01×10^{-2}).

3.1.3 *GC: Poor quality (PQ)*

As expected the PQ dataset had the smallest number of detected stars, at 445, this is ∼23% less than the AQ dataset and ∼47% less than the GQ dataset. As a reminder, Table 1 gives the median PSF FWHM for the PQ dataset, 82 ± 6.6 mas. This is ∼30 mas larger than the GQ PSF and ∼16 mas larger than the AQ PSF.

Similar to the previous GC datasets, the PQ results show a marginal improvement for the variable-PSF mode compared to single-PSF mode. The astrometric precision for variable-PSF mode ($\sigma_r \sim 1.32$ mas) is just 2% less than single-PSF mode ($\sigma_r \sim 1.35$ mas). A better improvement is seen in the photometric precision comparison; variable-PSF mode gives a precision of $\sigma_m \sim 0.042$ mag which is ∼10% smaller than the single-PSF mode precision ($\sigma_m \sim 0.047$). Finally, the average FVU measurement across all detected stars is once again quite similar between the two modes; variable-PSF gives an average FVU of 4.51×10^{-2} while single-PSF gives an average FVU of 4.64×10^{-2}.

3.2 *OB150029*

The microlensing target OB150029 is located in the least-crowded stellar field analyzed in this work, with a total of 63 stars cross-matched in at least five out of six frames. For this data, 10 reference stars were used for the initial PSF model. Coincidentally, this is the same amount of reference stars as the M53 dataset and is 60% fewer reference stars than the GC datasets. We note this dataset has the second-highest measured SR, and smallest FWHM of all datasets analyzed (Table 1). Additionally, as can be seen in Fig. 4(b), this dataset has the smallest variance in FWHM as measured across the field (∼6 mas).

For the microlensing target itself, the AIROPA analysis shows a modest improvement of ∼13% in the astrometric precision in variable-PSF mode ($\sigma_r = 0.223$ mas) over single-PSF mode ($\sigma_r = 0.252$ mas). Figure 9(a) shows the ratio of astrometric residuals for all stars detected in both PSF modes (binned by magnitude), OB150029 is shown by the red data point. The

photometric uncertainty and FVU evaluated on the target for both PSF modes are very similar, within 5% for single-PSF and variable-PSF modes. It should not be surprising that the PSF fitting errors and metrics are quite similar between single-PSF and variable-PSF for the target star in this case since the location of the target on the detector is nearly on-axis [Fig. 8(a)] and the PSF shapes are not significantly different for the static PSF and the central PSF from the variable-PSF mode. The residual images show effectively identical over-subtracted and under-subtracted features for both PSF modes [Figs. 8(b) and 8(c)]. We note there is an unrelated neighbor star ∼0.36 arcsec to the SW of the target, with a flux ratio of $f/f_{OB150029} \sim 0.1$. While the stellar profile of this fainter neighbor may have a small absolute effect on the SW wing of the OB150029 PSF, the magnitude of this effect will be the same for each case. Additionally, inspection of the residuals at the location of the nearby neighbor shows no statistically significant signal above or below the background noise in both cases.

Figure 9(a) shows the relationship (i.e., ratio) between the fitting metrics as a function of magnitude, and Table 3 reports the results for each metric and PSF mode. Generally, the same trend appears in the microlensing dataset as the GC datasets; a marginal improvement in the precision and fitting residuals in variable-PSF mode compared to single-PSF mode. The largest improvement is seen in both astrometric precision and FVU for variable-PSF mode, ∼10% smaller than the single-PSF mode results.

As a final test for this microlensing dataset, we performed an identical AIROPA analysis while omitting the target itself as a PSF reference star. Ideally, the results of such a test will reveal the influence (if any) that the target (i.e., brightest star in the field) has on the PSF modeling and extraction as well as the fitting parameters and residuals measured by the single-PSF and variable-PSF algorithms. The results of this reanalysis show indistinguishable results for the astrometric and photometric precision for the microlensing target ($\sigma_r = 0.223$ mas, $\sigma_m = 0.025$ mag), as well as an FVU value that is consistent (within 1σ) of the value measured while including the target as a PSF reference star.

3.3 M53

As described in Sec. 2.3, the two M53 datasets have significantly different data qualities. In particular, the PA 0 deg dataset has the largest variance in SR, FWHM, and RMS WFE of all data in this study. One cause of this is the observing window for the PA 0 deg data spans a time frame where the DIMM and MASS monitors recorded a particularly high seeing measurement [Fig. 1(b), green-colored data]. This is likely due to high cirrus cloud cover or other turbulent layers in the high-altitude atmosphere during two of the PA 0 deg exposures. A relatively small total number of PA 0 deg images were taken on the night (see Table 1 of Ref. 8), and the frames that correspond to the DIMM/MASS spike seen in Fig. 1 happen to be the images that have the most observed sources in common with the PA 90 deg images that were taken ∼1 h later in the same night. Because we want to maintain consistency amongst all datasets and to maximize the total number of cross-referenced stars in both PAs, we chose to keep all of the PA 0 deg frames for this particular dither position. This mostly affects the fainter stars in the field, as can be seen by comparing the limiting magnitudes in the PA 0 deg and PA 90 deg panels in Fig. 9. We note that AIROPA (and the Arroyo software) associates two PA 0 deg images with the large DIMM and MASS measurement.

3.3.1 M53 PA 0

A total of 98 stars were cross-matched across at least five of the six PA 0 deg frames, with 10 of the stars used to build the initial PSF model. The location and brightness of the selected PSF reference stars are given by the colored data points in the bottom panels of Fig. 5. The difference in astrometry, photometry, and FVU between single-PSF and variable-PSF modes largely follow the same trends seen in the GC and OB150029 analyses (Tables 2 and 3). Interestingly, the most significant difference for the M53 PA 0 deg single and variable PSF modes comes from the comparison of the photometric uncertainties [Fig. 9(c)]. The results show that the variable-PSF mode gives significantly lower photometric errors than the single-PSF mode (Table 3 columns 3–4 for M53 PA 0 deg).

It is worth noting a similar, yet less significant trend in photometric precision is also seen in the poorest quality GC data set (GC PQ). These trends suggest that for lower-quality, less uniform point sources, the spatially variable PSF model more precisely measures the intensity weighted integrated coordinate of the stars compared to the static PSF model. Additionally, the magnitudes and colors of the M53 stars as a function of off-axis location show a significant improvement in variable-PSF mode when comparing to an absolute HST reference (Sec. 3.3.3).

3.3.2 *M53 PA 90*

The higher quality PA 90-deg data has a total of 160 stars cross-matched in the images, with the same 10 stars used as PSF reference stars (lower-right panel of Fig. 5). Like the previous data sets, there is little to no improvement in the variable-PSF fitting metrics compared to the single-PSF results. The difference in stellar positions and magnitudes also follow similar trends seen in the previous data (Table 2). The average photometric error for all stars is ∼15% larger in the variable mode compared to single mode. The average astrometric error is nearly identical in both modes, at a ∼1% difference. The FVU values in both modes are within 1σ of each other (bottom row of Table 3).

Finally, we investigated the difference between astrometric residuals in both PSF modes after matching and transforming the PA 0-deg star list to the PA 90-deg list (and vice versa). We perform a first-order transformation using both stacked star lists from each PA as the master reference list and star list to be transformed in both cases. If the variable-PSF mode performs better, then we would expect astrometric residuals from this transformation process to be smaller for the spatially varying PSF mode, particularly for larger off-axis stars in the frames. Figure 10 shows the resulting astrometric quiver plots in the top panels, and the distribution and correlation between the astrometric residuals in both PSF modes in the bottom panels. The two distributions are very similar, and correlations largely follow the line of unity with a dispersion of ∼a few mas (bottom right panel of Fig. 10), which show that the astrometric residuals from the variable-PSF mode are not measurably smaller than the single-PSF residuals.
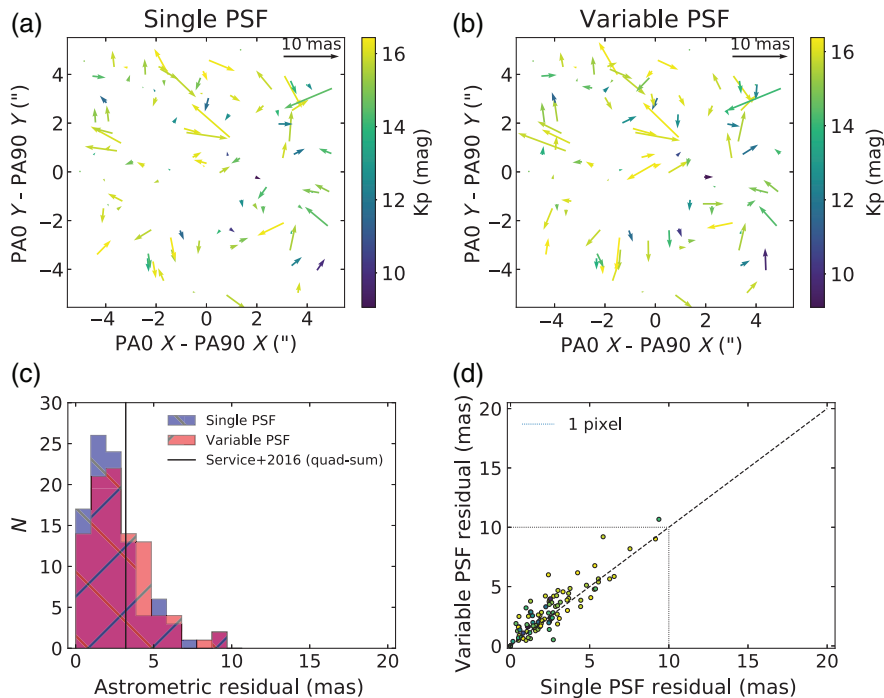
Fig. 10 (a) Quiver plot showing single-PSF astrometric residuals from the PA=0 → PA=90 transformation. (b) Same as (a), but for variable-PSF mode. (c) Distribution of astrometric residuals from both PSF mode transformations. (d) Correlation between astrometric residuals for both PSF modes, colored by Kp magnitude.
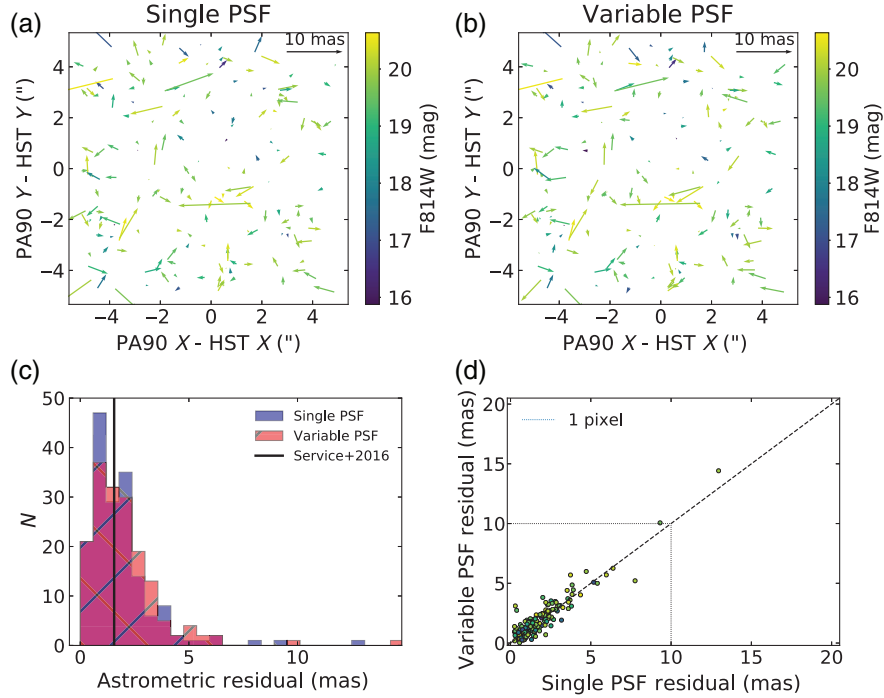
Fig. 11 Same as Fig. 10 but for stars transformed to HST. The color bar is given in F814W (Vega) magnitude. The vertical black line on the lower left panel shows the residual distortion calculated by Ref. 8.

3.3.3 HST cross reference

Both PA's star lists were independently transformed to an HST reference frame described in Sec. 2.3, with the same intention of examining the difference in astrometric residuals between single and variable modes. Figure 11 shows the PA 90-deg astrometric residual quiver plots in the upper panels, and corresponding distribution of astrometric residuals as well as the correlation between single-PSF and variable-PSF residuals in the lower panels. The distribution of astrometric residuals peaks at 1.52 mas in both PSF modes, this is consistent with the residual distortion on the NIRC2 detector that was found in Ref. 8 (denoted by the vertical black line in the bottom left panel of Fig. 11). The weighted mean and central 68% of both PSF mode distributions are given in Table 4. This table includes all variations of star list transformations that were performed on the M53 data sets (i.e., NIRC2, HST, and Gaia, described below).

Table 4 M53 astrometric residuals from NIRC2, HST, and Gaia.

Ref. Frame	N_{matched}	$\langle \sigma_{r_s} \rangle$ [mas]	$\langle \sigma_{r_v} \rangle$ [mas]
		PA 0	
PA 90	94	$2.53^{+1.59}_{-0.47}$	$2.82^{+1.67}_{-0.51}$
HST	90	$1.93^{+1.39}_{-0.44}$	$2.04^{+1.43}_{-0.45}$
Gaia	24	$7.61^{+2.76}_{-1.19}$	$7.35^{+2.71}_{-1.12}$
		PA 90	
PA 0	94	$2.43^{+1.56}_{-0.49}$	$2.89^{+1.70}_{-0.68}$
HST	157	$1.85^{+1.36}_{-0.43}$	$1.99^{+1.42}_{-0.45}$
Gaia	24	$7.39^{+2.72}_{-1.20}$	$7.80^{+2.79}_{-1.25}$

Further, we used the HST photometric measurements as an absolute standard to compare the NIRC2 single-PSF and variable-PSF photometry against. We do this by generating a color-magnitude diagram (CMD) for each PSF mode and PA, where we compare the HST I – Keck K color against the Keck K magnitudes for all cross-matched stars in each catalog. The NIRC2 data were photometrically calibrated to 2MASS Ks band magnitudes for this process. We cross-identify two bright stars in common between the NIRC2 data and 2MASS (2MASS J13125435 + 1810172 and 2MASS J13125408 + 1810194). From this cross-identification we calculate a zero-point offset of 3.70 and apply this to all stars in each catalog, including a calibration error of 0.06 magnitudes.

We then used the open-source package SPISEA[19] to generate a synthetic population for the cluster. We used parameters for the cluster age, metallicity, and mass fraction from Refs. [20] and [21]. We also adopted the extinction law of Ref. [22] when generating the population. The top panels of Fig. 12 show the single-PSF and variable-PSF CMDs. The data are colored by off-axis radial distance in the NIRC2 frames, and the best-fit isochrone from SPISEA is overlaid (black curve). Characteristic errors in color and magnitude for the CMDs are given by the vertical columns. There is a clear trend seen in the comparison between the CMD stars and the isochrone model in the single-PSF CMD. The difference in color between the stars and isochrone model shows a relatively strong dependence on radial distance in the NIRC2 frames. This same dependence is not seen in the comparison of the variable-PSF CMD and best-fit isochrone model. The lower panels of Fig. 12 show the color difference measurements (and errors) as a function of off-axis distance. A linear fit is made to each distribution, and the resulting slopes are 0.041 ± 0.008 mag arcsec^{-1} for single-PSF mode and -0.002 ± 0.009 mag arcsec^{-1} for variable-PSF mode. These results suggest roughly an order of magnitude improvement in the photometric performance of the variable-PSF mode compared to single-PSF mode. This marks the first
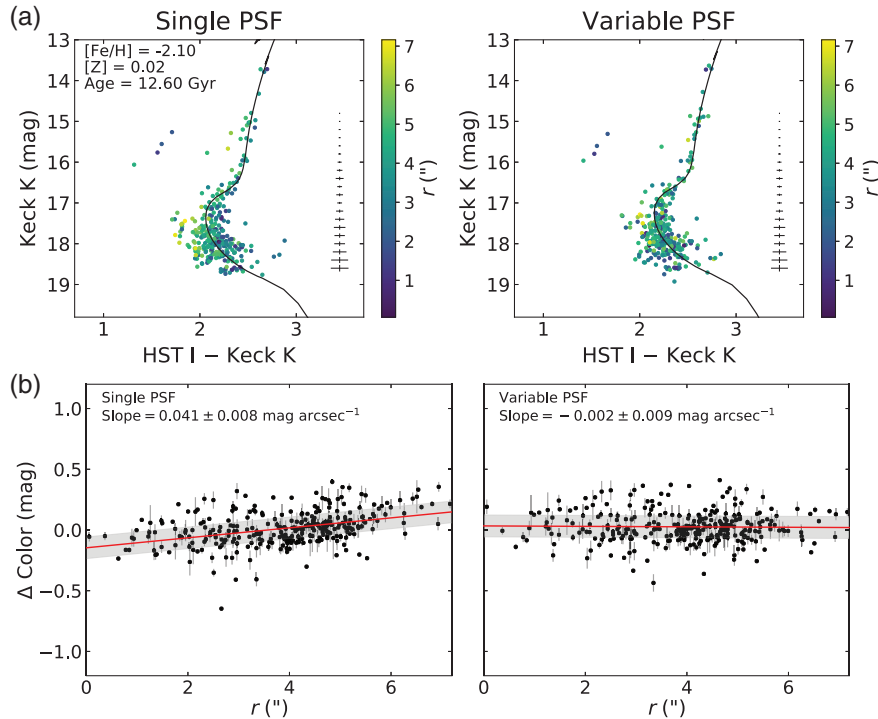

Fig. 12 (a) The M53 *HST I*–Keck *K* versus Keck *K* CMDs for both single-PSF and variable-PSF star lists. The solid black curve gives the best-fit SPISEA isochrone, with age, metallicity, mass fraction, and extinction from Refs. [20–22]. (b) The measured color index difference (i.e., empirical – isochrone) in single-PSF and variable-PSF modes as a function of off-axis radial distance. The solid red line shows the linear best-fit to each distribution, with the shaded gray region showing the 1σ spread around the best-fit. The distribution of color differences for single-PSF mode has a clear trend in radial distance, while the distribution is largely constant for variable-PSF mode.

definitive example of a significant improvement shown by variable-PSF mode over the single-PSF mode for on-sky science data.

3.3.4 *Gaia cross reference*

We continue our comparison of the single-PSF and variable-PSF catalogs by transforming both lists to the Gaia EDR3 catalog.[23] While Gaia has delivered exquisite astrometric data for over one billion sources now, there is a sizable fraction of spurious values reported by the instrument that are not so reliable. Recently, it has been shown that numerous astrometric solutions reported by Gaia suffer quite significantly for low signal-to-noise sources as well as for sources in crowded fields.[24] Given that the central region of M53 is crowded, we perform a careful investigation of Gaia astrometric quality flags for the stars cross-matched between NIRC2 and Gaia. A consideration that we make when matching the two PA's to Gaia is the astrometric fitting errors as described in Refs. 23 and 25. In particular, the "astrometric excess noise (ϵ)" parameter is described as the excess uncertainty that must be added in quadrature to obtain a statistically acceptable astrometric solution. Further, the excess term ϵ is introduced in order to effectively reduce the statistical weight of observations that may be affected by things like instrument and attitude modeling errors. Another error term we consider is the "astrometric excess noise significance," which is described as a dimensionless measure of the significance of the calculated ϵ. A value of >2 indicates that the reported ϵ is "probably significant."[26] Further details on these astrometric error terms can be found in Ref. 26.

Figure 13 shows the values reported by Gaia for the two astrometric error terms described above. The star symbols in the figure represent 32 NIRC2 stars that were cross-identified in Gaia. All other Gaia stars within a 30 arcsec radius of the center of the NIRC2 frame are plotted as well, and both distributions are colored by Gaia G magnitude. Given the higher astrometric precision in both the Keck and HST data, we choose to make a cut on the Gaia stars at $\epsilon < 5$ mas and significance <2 (shaded regions in Fig. 13), which leaves 24 remaining Gaia stars (unshaded region) that are used for the final transformation. As a note, we tested more strict and less strict cutting thresholds for this process (i.e., some stars rejected by their significance value) and found similar results for each scenario. The cut at $\epsilon < 5$ mas left a sufficient number of stars needed for a reliable first-order transformation, while rejecting likely astrometric outliers (which are mostly faint, low-SNR stars).
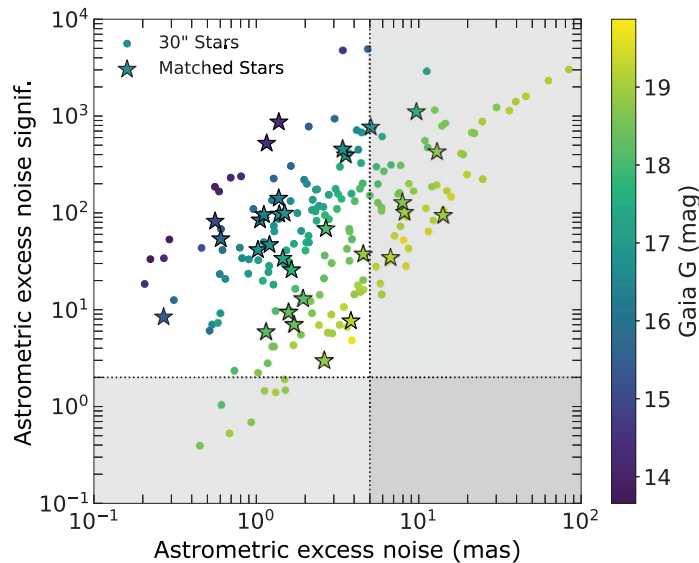
Fig. 13 Astrometric excess noise significance versus astrometric excess noise as a function of Gaia *G* magnitude in the 30 arcsec field surrounding the center of the NIRC2 images. The reference stars used for the NIRC2 → Gaia transformation are marked as star symbols. Dotted vertical and horizontal lines denote the noise and noise significance thresholds used to cut reference stars.
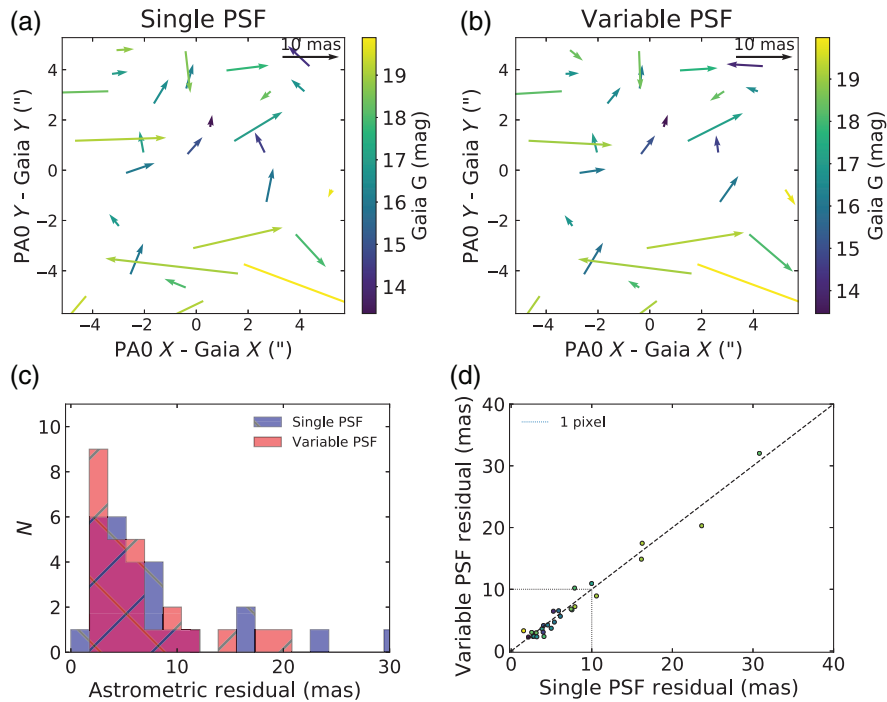
Fig. 14 Same as Figs. 10 and 11 but for stars transformed to Gaia EDR3. The color bar is given in Gaia G magnitude.

The quiver plots in the top panels of Fig. 14 show the 2D astrometric residuals after transforming the PA 0 deg stars to the Gaia reference frame. The distribution of astrometric residuals for both PA's peaks at $\sigma_r \sim 5$ mas, and the faintest stars have the largest residuals, as expected. Table 4 shows the weighted mean for each distribution, where the mean and errors are largest for Gaia. As described earlier, there are several reasons why the Gaia residuals are largest — generally, the Gaia astrometric precision is worse than HST (and NIRC2), especially for crowded field sources. The astrometric excess noise and other error terms contribute overall larger residuals when transforming NIRC2 into the Gaia reference frame. Finally, the calculation of the weighted mean and central 68% of the distribution is more significantly affected by the spread in residuals (and possible outliers) for the much smaller Gaia data set (24 stars).

3.4 Expected Performance and Comparison to Simulations

The expected reduction in astrometric and photometric uncertainties for variable-PSF mode was not seen for the on-sky datasets considered in this work. As described in Ref. 7, for simulated data (e.g., fiber sources and the simulated GC scene), the photometric and astrometric residuals were significantly reduced (by 80% on average in variable-PSF mode). In contrast, our on-sky results show an improvement in variable-PSF mode of only 15% in the best case. Figures 11–17 of Ref. 7 show simulation results, including comparisons of photometric and astrometric residuals, as well as the FVU values for single-PSF versus variable-PSF modes.

In more detail, the simulated GC scene analyzed in Ref. 7 shows a positional accuracy improvement from 8.3×10^{-1} mas (single) to 1.7×10^{-1} mas (variable). The photometric accuracy improved from 3.7×10^{-2} mag (single) to 0.6×10^{-2} mag (variable). Our best-quality, on-sky GC (GC GQ) results show only a small reduction in astrometric and photometric accuracy of 8.15×10^{-1} mas (single) to 8.06×10^{-1} mas (variable) and 3.64×10^{-2} mag (single) to 3.62×10^{-2} mag (variable), respectively. In the GC simulations, the median FVU for variable-PSF mode is 6.2×10^{-5}, significantly better than the single-PSF value of 5.7×10^{-4}. Again, our best on-sky GC results show identical median FVU values between both PSF modes for all stars as well as only bright stars (5.0×10^{-3} for bright stars in both modes). Finally, since the study of Ref. 7 shows similar improvement (e.g., same order of magnitude) in residuals between a sparse

field of fiber sources and the simulated GC scene, then similar improvements are to be expected in the case of OB150029 and M53.

4 Discussion and Conclusion

We have analyzed several on-sky NIRC2 datasets with the single PSF mode and spatially variable PSF mode in AIROPA. We find that the performance of AIROPA is reliable across different conditions including poor, average, and good quality seeing, crowded or sparse stellar fields, varying numbers and brightnesses of PSF reference stars, and in different telescope PA's.

Our analysis of the datasets largely shows only a marginal improvement in photometric or astrometric residuals between the static PSF model and spatially variable PSF model within AIROPA. A comparison of the FVU metric between the two modes shows similar results. This implies that the ability of AIROPA to reconstruct the PSF for a wide range of on-sky data remains limited by unaccounted for static or quasistatic aberrations in the telescope. We also show that the effect of varying atmospheric conditions, number and spatial location of selected PSF reference stars, and telescope PA do not have a significant effect on the performance of AIROPA in either of the modes.

One metric that does show a significant improvement in the variable-PSF mode over the single-PSF mode is a comparison of the color spread of M53 stars in a Keck + *HST* CMD. We find a measurable trend in photometry as a function of off-axis location in the single-PSF mode star catalog, whereas the variable-PSF mode star catalog shows no trend. After comparing the fitted trend line for each case, we find that the systematic photometric trend is reduced by ∼10× for the spatially variable PSF mode. This represents the first significant improvement from the variable-PSF mode that has been found for on-sky science data, which implies that the historically difficult to obtain absolute photometry with Keck can be reliably measured in the variable-PSF mode.

Comparing the FVU metrics between PSF fitting modes across all datasets shows at best an ∼5% improvement in bright stars for the spatially varying PSF model over a static PSF model. This is significantly less than what has been shown in tests on simulated GC data.[7] For OB150029 we measure an astrometric precision that is ∼13% smaller for the variable-PSF mode over the single-PSF mode. However, the FVU metric for this target does not follow the same improvement seen in the astrometry. For the M53 data, we find that the astrometric residuals between single and variable-PSF modes are quite similar when transforming a stack of PA = 0-deg frames onto the PA = 90-deg reference frame. Further, when transforming the two PA's to the Gaia and HST reference, we find comparable astrometric residuals in both PSF modes.

Finally, for most of the fitting metrics (except for the Keck + HST photometric comparison), we largely confirm the result of Ref. 7 which shows no significant improvement in fitting residuals for the spatially variable PSF mode in AIROPA with on-sky data. It is hypothesized that there remain static or quasistatic instrumental aberrations that persist in the telescope, which are not included in afternoon phase-diversity measurements because the up-stream telescope optics are not part of this calibration. This hypothesis is backed up by a recent analysis that shows a dominant source of error in the PSF comes from primary segment misalignments (O. Beltramo-Martin, personal communication). The work shows several hundred nm of wavefront error (WFE) coming from the primary piston segments, which can become misaligned as quickly as hours after initial alignment. Currently, the Keck-II primary mirror segments are realigned every 2-weeks, however, these results suggest the cadence may need to be increased in order to minimize any contribution to the PSF error from this primary segment phasing. Future on-sky phase-diversity measurements should help in identifying the source(s) of instrumental aberrations that are not currently accounted for in fiber phase-diversity measurements.

Acknowledgments

References

1. P. Wizinowich et al., "Keck all sky precision adaptive optics," *Proc. SPIE* **11448**, 114480E (2020).
2. C. Z. Bond et al., "Adaptive optics with an infrared pyramid wavefront sensor at keck," *J. Astron. Telesc. Instrum. Syst.* **6**(3), 039003 (2020).
3. T. Do et al., "Point-spread function reconstruction for integral-field spectrograph data," *Proc. SPIE* **10703**, 107030I (2018).
4. G. Witzel et al., "The airopa software package: milestones for testing general relativity in the strong gravity regime with AO," *Proc. SPIE* **9909**, 99091O (2016).
5. A. Ciurlo et al., "Airopa ii: modeling instrumental aberrations for off-axis point spread functions in adaptive optics," *J. Astron. Telesc. Instrum. Syst.* **8**(3), 038007 (2022).
6. M. Britton, "The anisoplanatic point-spread function in adaptive optics," *Publ. Astron. Soc. Pac.* **118**(844), 885 (2006).
7. P. Turri et al., "Airopa III: testing simulated and on-sky data," *J. Astron. Telesc. Instrum. Syst.* **8**(3), 039002 (2022).
8. M. Service et al., "A new distortion solution for NIRC2 on the keck ii telescope," *Publ. Astron. Soc. Pac.* **128**(967), 095004 (2016).
9. A. Ghez et al., "Measuring distance and properties of the milky way's central supermassive black hole with stellar orbits," *Astrophys. J.* **689**(2), 1044 (2008).
10. J. Lu et al., "A disk of young stars at the galactic center as determined by individual stellar orbits," *Astrophys. J.* **690**(2), 1463 (2008).
11. https://galacticcenter.astro.ucla.edu/
12. A. Ghez et al., "Stellar orbits around the galactic center black hole," *Astrophys. J.* **620**(2), 744 (2005).
13. T. Do et al., "Relativistic redshift of the star s0-2 orbiting the galactic center supermassive black hole," *Science* **365**(6454), 664–668 (2019).
14. A. K. Gautam et al., "An adaptive optics survey of stellar variability at the galactic center," *Astrophys. J.* **871**(1), 103 (2019).
15. S. Jia et al., "The galactic center: Improved relative astrometry for velocities, accelerations, and orbits near the supermassive black hole," *Astrophys. J.* **873**(1), 9 (2019).
16. A. Udalski et al., "The optical gravitational lensing experiment," *Acta Astron.* **42**, 253–284 (1992).
17. J. R. Lu et al. (in prep).
18. J. Anderson et al., "The acs survey of globular clusters. v. generating a comprehensive star catalog for each cluster," *Astron. J.* **135**(6), 2055 (2008).
19. M. W. Hosek, Jr et al., "Spisea: a Python-based simple stellar population synthesis code for star clusters," *Astron. J.* **160**(3), 143 (2020).
20. A. Dotter, A. Sarajedini, and J. Anderson, "Globular clusters in the outer galactic halo: new Hubble space telescope/advanced camera for surveys imaging of six globular clusters and the galactic globular cluster age–metallicity relation," *Astrophys. J.* **738**(1), 74 (2011).
21. R. Wagner-Kaiser et al., "Bayesian analysis of two stellar populations in galactic globular clusters. ii. NGC 5024, NGC 5272, and NGC 6352," *Astrophys. J.* **826**(1), 42 (2016).
22. E. F. Schlafly, et al., "The optical-infrared extinction curve and its variation in the milky way," *Astrophys. J.* **821**, 78 (2016).

23. Gaia Collaboration et al., "Gaia early data release 3. Summary of the contents and survey properties," *Astron. Astrophys.* **649**, A1 (2021).
24. J. Rybizki et al., "A classifier for spurious astrometric solutions in GAIA EDR3," *Mon. Not. R. Astron. Soc.* **510**(2), 2597–2616 (2022).
25. Gaia Collaboration et al., "Gaia data release 2-summary of the contents and survey properties," *Astron. Astrophys.* **616**, A1 (2018).
26. L. Lindegren et al., "The astrometric core solution for the gaia mission-overview of models, algorithms, and software implementation," *Astron. Astrophys.* **538**, A78 (2012).

Sean K. Terry is a postdoctoral scholar at University of California, Berkeley, in the Astronomy Department. His interests are in adaptive optics, PSF reconstruction, and gravitational microlensing. He is currently a science team member on the KAPA project at Keck Observatory and is also involved in preliminary survey design for the Nancy Grace Roman Space Telescope's Galactic Bulge Time Domain Survey.

Jessica R. Lu is an associate professor at University of California, Berkeley, in the Astronomy Department. His expertise is in adaptive optics, astrometry, stellar populations and dynamics, gravitational microlensing, and black holes. He is the project scientist for adaptive optics projects including `IMAKA on the University of Hawaii 2.2 m telescope and KAPA at the Keck Observatory.

Biographies of the other authors are not available.